JOM
https://doi.org/10.1007/s11837-023-06084-y

Phase Formation of a C6 Niobium Hemicarbide from Sub-stoichiometric NbC

ILIAS BIKMUKHAMETOV,[1,2] JONATHAN L. PRIEDEMAN,[1] LIURUKARA D. SANJEEWA,[3,4] CHRISTOPHER R. WEINBERGER,[5,6] and GREGORY B. THOMPSON [1,2,7]

1.—Department of Metallurgical and Materials Engineering, The University of Alabama, Tuscaloosa, AL 35487, USA. 2.—Alabama Analytical Research Center, The University of Alabama, Tuscaloosa, AL 35487, USA. 3.—University of Missouri Research Reactor (MURR), University of Missouri, Columbia, MO 65211, USA. 4.—Department of Chemistry, University of Missouri, Columbia, MO 65211, USA. 5.—Department of Mechanical Engineering, Colorado State University, Fort Collins, CO 80523, USA. 6.—School of Advanced Materials Discovery, Colorado State University, Fort Collins, CO 80523, USA. 7.—e-mail: gthompson@eng.ua.edu

The niobium hemicarbide (Nb_2C) has at least three known polymorphs: α (Pnma or Pbcn), β ($P\bar{3}1m$), and γ ($P6_3/mmc$) as a function of temperature. Identification of these phases has been notoriously difficult particularly for the lower-temperature variations (α and β) because of their long-range vacancy ordering. In the current study, an overall Nb_2C composition has been processed by hot isostatically pressing NbC and Nb powders together which did not fully homogenize. Using neutron diffraction and selected area electron diffraction, the C6 ($P\bar{3}m1$) structure was identified in the Nb_2C. The formation pathway for this phase is postulated from the high density of stacking faults observed in the NbC.

INTRODUCTION

Niobium carbides are of interest as engineering materials because of their high melting temperatures and high hardness, making them ideal candidate ceramics for applications in extreme environments.[1] The properties of these niobium carbides are strongly dependent on the carbon concentration, as their phase stability to different structures exists over a wide range of carbon compositions.[2,3] Thus, it is critical to understand the structures that form in this system both as a function of composition as well as processing parameters.

Of the studies that have examined phase stability in the niobium carbide system,[4–9] they agree to the existence, without question, of the NbC and Nb_2C phases, with the former being the B1 ($Fm\bar{3}m$) rocksalt structure where NaCl is the prototype. This structure is stabilized up to the highest melting temperature point for all niobium carbides and can accommodate sub-stoichiometric, metal-rich compositions with increasing temperature. However, in the lower-temperature regimes, experimental and theoretical studies point to the existence of vacancy-ordered forms, such as Nb_6C_5,[4,5,9] Nb_4C_3, and Nb_3C_2.[4,5,9–12]

While there is universal agreement that the Nb_2C phase exists, it has as many as three reported polymorphic structures as a function of temperature.[13–20] The low-temperature or α -Nb_2C is reported to be either ζ-Nb_2C structure (Pnma) or ζ-Fe_2N (Pbcn), and is stabilized at $T < \sim 1200$ K. Between ~1200 and ~1800 K, the intermediate-temperature ε-Fe_2N ($P\bar{3}1m$) structure forms, and, above ~1800 K, the $L'3$ structure ($P6_3/mmc$) is stabilized. The correct identification of the carbon atom ordering as well as the sluggish kinetics associated with atomic ordering has created substantial difficulties in correctly identifying these lower-temperature α and β phases, their compositional ranges, and the temperatures where they exist. This has been noted by Smith et al.[20] and Vishwanadh et al.,[17] who each commented that subtle changes in diffraction spots and/or shifts in

(Received May 18, 2023; accepted August 11, 2023)

Published online: 05 September 2023

reflections were required for structure determination clarity. To readily identify ordering on the carbon sublattice, neutron diffraction, and selected area electron diffraction are considered the most viable methods as compared to x-ray diffraction.[21,22] The former, neutron scattering, is from the atomic nucleus whereas x-ray diffraction is from the electron cloud, which is less sensitive in identifying vacancy ordering.

In this study, we provide a detailed neutron and electron diffraction investigation to identify the structure of Nb_2C produced by the hot isostatic pressing reaction between NbC and Nb powders. This investigation aims to understand how the NbC undergoes phase transformations as it serves as the carbon reservoir for the reaction. In a prior report by Smith et al.,[20] this reaction pathway was investigated between these two powders, but it mainly addressed how the carbon reacted with the Nb powder converting it to the ε-Fe_2N structure. This paper now focuses on the decomposition of the NbC as it converts to the niobium hemicarbide.

METHODOLOGY

Sample fabrication

The niobium hemicarbide was fabricated by blending commercial Nb (ABCR, $<$ 45 μm, 99.8 %) and NbC (ABCR, $<$ 1.1 μm, 99.7 %) powders into an overall $NbC_{0.56}$ composition. The mixed powder was pressed into a niobium canister under an inert gas environment inside a glove box. The canister was then outgassed using a heating plate while under evacuation that was then hermetically sealed by welding the canister closed and performing a helium leak check. The canister was hot isostatic pressed (HIP) in an argon atmosphere for 60 min at ~1800°C under 205 MPa. The canister was furnace cooled at ~ 27°C/min to room temperature, whereupon the consolidated billet was removed from the cannister using a diamond cutting saw. The composition was confirmed through thermo-combustion analysis of the post-HIP sample using a certified commercial vendor (Northern Analytical).

Electron Microscopy

Post-consolidation, the billet was sectioned and polished using various SiC papers with increasing grit sizes to 1200, followed by polishing with a 0.04-μm diamond suspension. A final vibratory polish using a 0.02-μm colloidal silica suspension provided a mirror surface. The sample was imaged by scanning electron microscopy (SEM) using a Thermo Fisher Scientific Apreo FEG-SEM, whereupon electron back-scatter diffraction (EBSD) for phase and grain orientation was captured with the EDAX EBSD platform attached to the microscope. The SEM-EBSD settings were collected at 20 keV, a beam current of 1.6 nA, and at a scan step size of 10 μm. TSL OIM v.8 software analyzed the acquired EBSD dataset. Site-specific transmission electron microscopy (TEM) foils were extracted based on the SEM-EBSD-identified locations of the phases, using a focus ion beam (FIB) lift-out method, with further details found in reference.[23] Here, the FIB milling was carried out in a Tescan Lyra FIB-SEM, and the TEM was performed in a FEI Tecnai F20 (S)TEM at 200 keV. Simulated selected area electron diffraction patterns were computed using SingleCrystal v.4.1.9.

Neutron Diffraction

Neutron diffraction was performed at the University of Missouri Research Reactor using a position-sensitive detector powder diffractometer. A double-focusing Si(511) monochromator produced a neutron wavelength of λ = 1.48098 Å with the instrument using an oscillating radial collimator. The diffracted data was collected from 30° to 105° 2Θ at room temperature, with the neutron diffraction dataset analyzed using the FullProf Suite Package.[24]

Density Functional Theory Simulations

To refine the previous first principal ab initio calculations,[9] and make direct comparisons of the cohesive energies between different structures of the niobium hemicarbides, we utilized density functional theory (DFT) using a plane wave basis as implemented in the Vienna Ab-Initio Simulation Package.[25,26] The core electrons simulated were the $4s^2 4p^6 4d^4 5s^1$ in Nb and the $2s^2 2p^2$ in C, while the interactions between the core and valence electrons were modeled using the projector augmented wave method.[27,28] The exchange–correlation energies were evaluated using the generalized gradient approximation parameterized by Perdew, Burke, and Ernzerhoff.[29] The total energies were found to be converged with a plane wave cutoff energy of 600 eV with the Brillouin zone integration of $20 \times 20 \times 11$ used and scaled to ensure a constant mesh density in reciprocal space.

RESULTS AND DISCUSSION

Phase Stability

The neutron diffraction results are plotted in Fig. 1a as a thick gray line with a Gaussian (normal) distribution for each major peak outlined by a thinner black line. Beneath these curves are various space group {hkl} reflections for the niobium (hemi)carbide crystal structures, which are color coded to the legend shown in the same figure. As many different structures exist, with their different space groups, we have provided a quick reference table of structure types and space groups in Table I. These structures are taken from the known phases as well as others that have been computationally investigated as possible structures.[9] Furthermore, we direct the interested reader to reference,[4] which

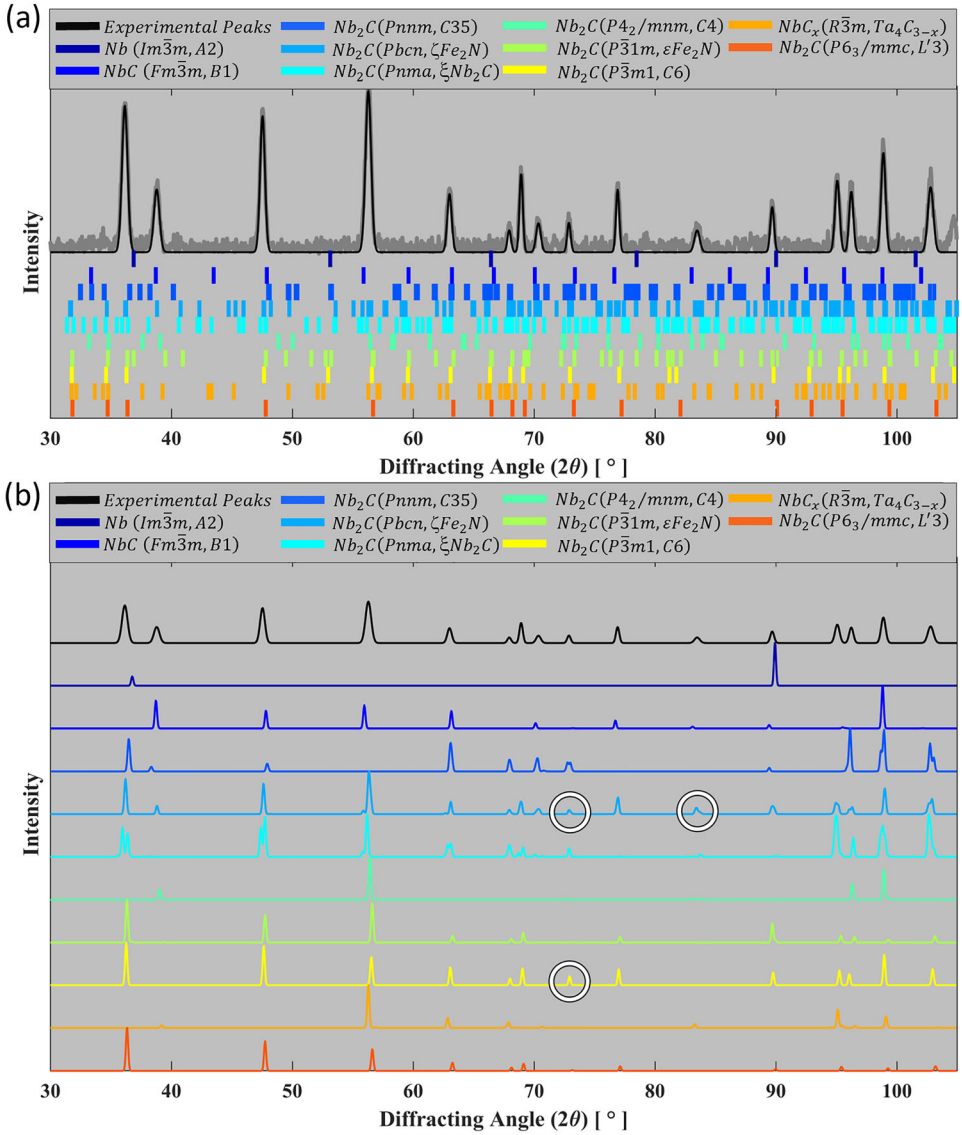

Fig. 1. (a) Raw neutron diffraction pattern (thick grey line), simplified diffraction pattern using Gaussian-distribution peak fits (thin black line), and exact reflection angles for various niobium (hemi)carbide crystal structures. (b) Comparison of experiment peaks with combined peaks for the considered niobium (hemi)carbide structures. Combined peaks that uniquely correlate to experimental peaks ("tells") are circled. The legend contains the space group as well as the (prototype) structure of the Nb_2C (Color figure online).

is a review article on the various phase stability and crystallography constructs for the transition metal carbides, since multiple Me_2C structures will be discussed here. For brevity and consistency, we use the terminology of *data* to refer to the direct experimental scattering results (i.e., the thick gray line), *reflections* to refer to higher intensity diffraction signals from the scattering results, and *peaks* to indicate the use of the Gaussian normal fits to these reflections at a predicted scattering angle.

The amount of information presented in Fig. 1a can make distinguishing the subtle differences in the niobium hemicarbide structures difficult. Therefore, to facilitate phase identification, we have placed Gaussian distributions at each predicted reflecting angle and multiplied the resulting "predicted diffraction pattern" by the experimentally-based fitted pattern, with additional information concerning this procedure provided in the appendix, Fig. 6. Figure 1b is a compilation of all the combined peak curves together, which allows for improved isolation of the various potential niobium hemicarbide structures. From Fig. 1b, the B1 NbC structure can be identified, while the other peaks match one or more of the various niobium hemicarbides, indicating that the specimen is a multi-phase niobium carbide. While the overall composition of this sample would place it in a niobium hemicarbide single-phase field, the consolidation reaction of the NbC and Nb powders did not result in homogenization, although no elemental Nb is detected. This multi-phase microstructure was previously noted by

Table I. Compatibility table of the niobium hemicarbides to their respective space group and associated prototype structure

			Atom site occupancy					
	Space Group	**Structure**	**Atom type**	**Wycoff**	**x**	**y**	**z**	**Ref.**
α-Nb_2C	Pnma	ζ-Nb_2C	C	4c	0.1203	0.25	0.013	18
			Nb	4c	0.2842	0.25	0.2934	
			Nb	4c	0.4644	0.25	0.7311	
α- Nb_2C	Pbcn	ζ-Fe_2N	Fe	8d	0.249	0.128	0.0827	30
			N	4c	0	0.364	0.25	
β- Nb_2C	$P\bar{3}1m$	ε-Fe_2N	Nb	6k	0.3333	0	0.25	31
			C	2d	0.3333	0.6666	0.5	
			C	1a	0	0	0.0	
γ- Nb_2C	$P6_3/mmc$	L'3	C	2a	0	0	0	32
			Nb	2c	0.3333	0.6666	0.25	
Nb_2C	$P\bar{3}m1$	C6	Nb	2d	0.3333	0.6666	0.28	33
			C	1a	0	0	0	
Nb_2C	Pnnm	C35	Cl	4g	0.275	0.35	0	34
			Ca	2a	0	0	0	
Nb_2C	$P4_2/mnm$	C4	Cl	2a	0	0	0	34
			Ca	4f	0.3047	0.3047	0	
Nb_4C_{3-x}	$R\bar{3}m$	Ta_4C_{3-x}	C	6c	0	0	0.085	35
			Nb	6c	0	0	0.2082	
			Nb	6c	0	0	0.3753	
			C	3b	0	0	0.5	
			C	3a	0	0	0	
NbC	$Fm\bar{3}m$	B1	Nb	4a	0	0	0	36
			C	4b	0.5	0.5	0.5	
Nb	$Im\bar{3}m$	A2	Nb	2a	0	0	0	37

the authors of reference[20] and will be further confirmed in subsequent electron microscopy imaging of the microstructure. This also highlights that direct sintering of a metal and metal carbide powder is insufficient for complete homogenization for these HIP conditions; in contrast, the reduction of metal oxides to carbides has shown promise in the homogenization of multi-component carbides and may be a more viable processing route.[38]

To determine the niobium hemicarbide phase(s), we have compared the experimentally determined peaks with those determined from the theoretical structures. We first consider the ζ-Nb_2C structure (Pnma), i.e., the turquois-colored line. This phase yields a doublet reflection near 36° 2Θ, whereas all other niobium hemicarbides have a single reflection at this diffraction angle. The absence of the doublet reflection in the experimental data suggests that this structure is not the dominant hemicarbide phase. Of the remaining niobium hemicarbides, many of these structures have similar diffraction peak locations that trend with the experimental data. However, three specific peaks stand out for clarification in the phase identification, which have been circled in Fig. 1b and referred to as "tells."

At a diffraction angle near 73° 2Θ, a clear experimental diffraction peak is present that matches a similar reflection for the ζ-Nb_2C structure, but this structure has been dismissed because of the lack of the doublet reflection at the lower scattering angle discussed in the previous paragraph. The other structures at this angle are the ζ-Fe_2N (Pbcn) and/or the C6 ($P\,\bar{3}m1$) structures. While one could use the experimental diffraction peak at approximately 84° 2Θ to match the ζ-Fe_2N structure and eliminate the C6 structure, this scattering angle also matches a reflection for B1 NbC, and the sample is a multi-phase microstructure. Hence, one cannot definitively dismiss C6. While there are relative differences in the intensities for the reflections that could further guide a decision, the neutron diffraction was taken from the consolidated billet and not randomly orientated powders, which would eliminate texture bias in using intensities. Hence, the location of the peaks, rather than the intensity of the peak, is used as the identifying marker for structure determination.

While the neutron diffraction data provide insight into the possible dominant niobium hemicarbide structure(s), it is not definitive in its identification. The work of Smith et al.[20] demonstrated that the local crystal structures in the niobium carbides can be determined using selective area electron diffraction (SAED), which we will use here to provide further investigation. Figure 2a is a FIB ion contrast image with a marked rectangular region,

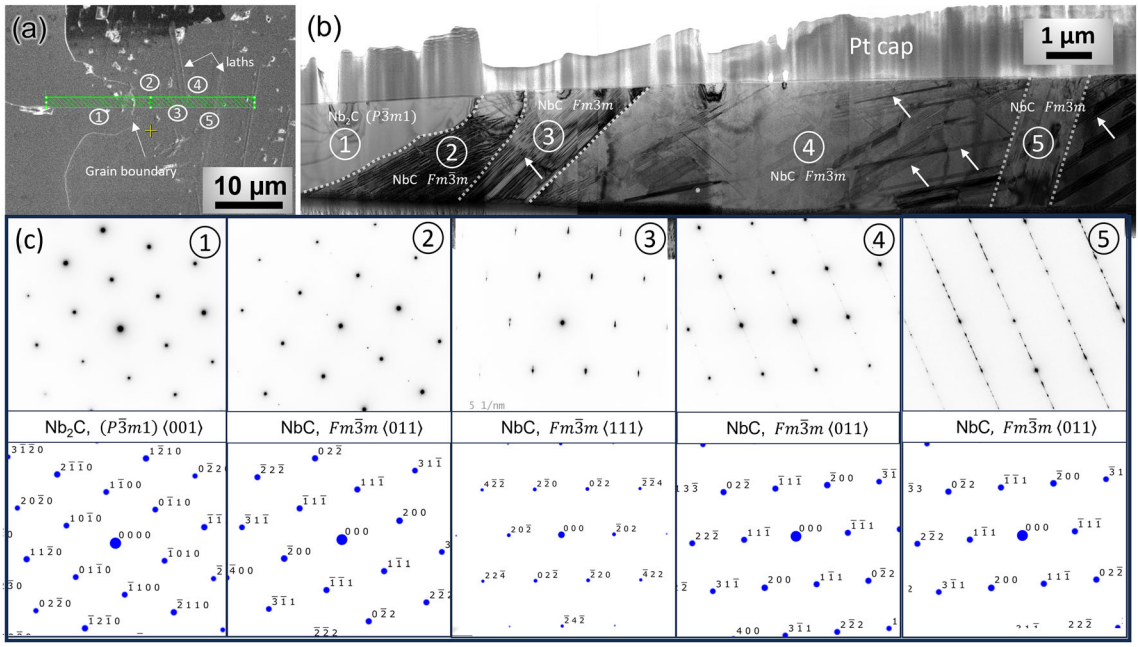

Fig. 2. (a) FIB ion contrast image of $NbC_{0.56}$ sample outlining the region of lift-out for TEM analysis; (b) Bright-field TEM image of the sample from the region in (a), numbers indicate the corresponding regions in (a); (c) SAED patterns for each region with matched simulated patterns for each region. Note that the lack of additional reflections in the SAED patterns in regions 2 and 3 as compared to region 5 is a consequence of the latter region is aligned to a zone axis where the stacking faults were excited.

whereupon a TEM foil will be extracted. This rectangular region spans a grain boundary and laths within the microstructure, with these features indicated by the arrows and labeled text in this same figure. Figure 2b is a compiled image of TEM micrographs that span the TEM foil from (a), with different microstructural regions labeled 1–5. SAED patterns are provided under each region and were used for phase identification of that region. Region 1 was indexed to the C6 Nb_2C structure, which would be a match to the neutron diffraction in Fig. 1; however, as this C6 structure, to the authors' knowledge, has not been reported for the niobium hemicarbide, we will return to it with a more thorough diffraction series analysis. Regions 2–5 are indexed to the B1 NbC structure. The presence of stacking faults is evident in the B1 NbC regions. In regions 2, 3, and 5, these faults appeared to be primarily along a single parallel close-packed plane (solid line arrows) while, in region 4, we noted that these faults are crisscrossed on multiple close-packed planes (dashed line arrows).

To determine if indeed the Nb_2C grain in region 1 in Fig. 2a is C6, we have compared the diffraction patterns taken at two different zone axes to this structure and other potential structures, as shown in Fig. 3. The various simulated diffraction patterns for each of these structures were selected based on the best match to the symmetry of the experimental acquired pattern. For the first zone axis, Fig. 3a, the starred makers for the simulated patterns are for C35 (Pnnm), *L*'3 ($P6_3/mmc$), C4 ($P4_2/mnm$), and the C6 ($P\bar{3}m1$), and each pattern provided the closest match to the experimental pattern. However, by using the neutron diffraction results, we can eliminate C35 and *L*'3 as the structure. Other hemicarbide patterns were also dismissed by the lack of specific reflection matching between the simulation and the experimental SAED pattern, i.e., ζ-Nb_2C and ε-Fe_2N. While the neutron diffraction pattern (Fig. 1) allowed the ζ-Fe_2N structure to be a candidate for consideration, at least for this particular grain, the SAED pattern is not a good fit to this structure, as indicated by the missing reflections in the experimental pattern as compared to the simulated pattern, where the arrows in the simulated pattern indicate the location where these additional reflections should be observed. This would leave either the C4 or C6 structures based on the SAED, but C4 was not a match to the neutron diffraction.

To further confirm that this grain in Fig. 2b's region 1 has the C6 structure, the foil was tilted to another zone axis and the SAED pattern was collected in Fig. 3b. Again, we compare this experimental pattern to each of the various hemicarbide structures. In this orientation, neither the C35 nor *L*'3 structures match, while they were candidates in Fig. 3a. This new zone axis' diffraction pattern confirms their dismal. This new zone axis now shows that the C6 and ε–Fe_2N structures are candidate matches. However, the ε–Fe_2N structure was not a match to the prior zone axis in Fig. 3a. Likewise, the stereographic tilt from the experimentally determined tilt angles of α and β in the

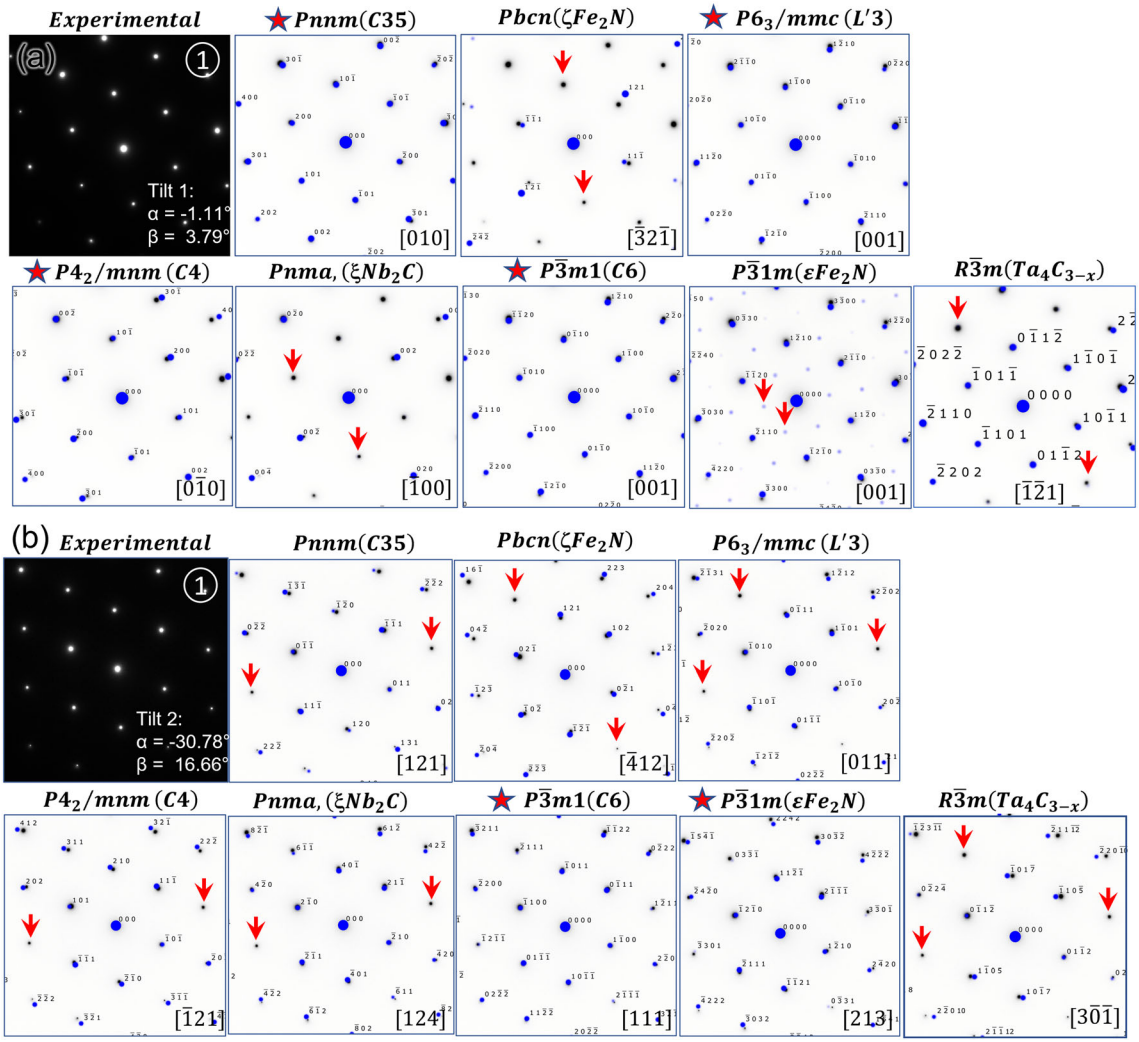

Fig. 3. TEM bright field image where phase identification of the Nb_2C in region 1 in Fig. 2 was conducted by selected area electron diffraction (SAED) technique along with different simulated patterns. The star designates the best fits to the simulated experimental pattern and the red arrows indicate reflections in the simulation not captured in the experimental pattern. (a) Zone axis 1 and (b) Zone axis 2. Blue are the simulated diffraction spots and the black are the experimental spots, having their contrast inverted from the experimental image (Color figure online).

TEM between the C6 [001] to [111] zones is self-consistent. Hence, the niobium hemicarbide, for this grain, has the C6 structure. While this provides evidence for the C6 existence, we do note that the TEM was taken from a selected region and that the neutron diffraction provides an average diffraction collection from multiple grains. Since there are significant peak overlaps for previously confirmed niobium hemicarbide phases,[4] and even prior work by the authors has noted the ε–Fe_2N structure by electron diffraction in this sample,[20] with the ε–Fe_2N phase fully consistent with the neutron diffraction results, we do not conclude that C6 is the only hemicarbide structure in this consolidated billet.

With the C6 structure confirmed, we now investigate how it could precipitate. Figure 4a is an EBSD phase map that shows the location for a site-specific TEM foil extraction between a Nb_2C phase (green) precipitating out of a NbC grain (red), with several interfaces being captured in the planned FIB-milled lamella (Fig. 4b). In Fig. 4c, the TEM bright field image shows distinct bands of NbC, Nb_2C, and faulting, like those seen in Fig. 2. The faulted region is further confirmed by the linear alignment of multiple, closely spaced diffraction reflections in the SAED pattern from region 3 in the same Fig. 4c. Note that the circled regions for 1, 2, and 3 represent the general area where the analysis was taken, but do not represent the selected area aperture used for any imaging or diffraction; rather, they are provided as a guide to link which features are tracked between each image.

The C6 structure is a stacking fault-derived structure and has been reported to be the low-temperature stable structure for the tantalum

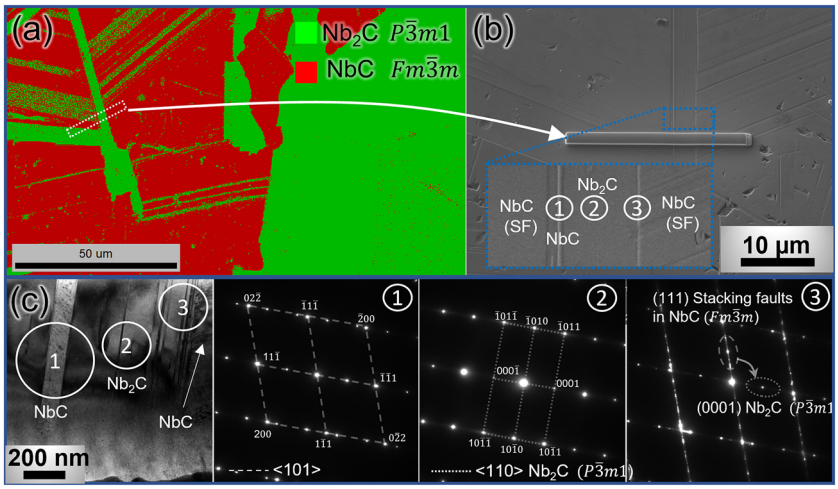

Fig. 4. (a) EBSD phase map with image quality map inset showing different phase regions in $NbC_{0.56}$ sample; (b) SEM image of $NbC_{0.56}$ lift-out 2 sample, outlining the region of lift-out for TEM analysis; (c) Bright-field TEM image of the sample from the magnified region in (b), numbers indicate the corresponding regions in (b) and diffraction patterns from these regions. Note that regions labeled 1, 2, and 3 are from the same general area located for each region in each image (Color figure online).

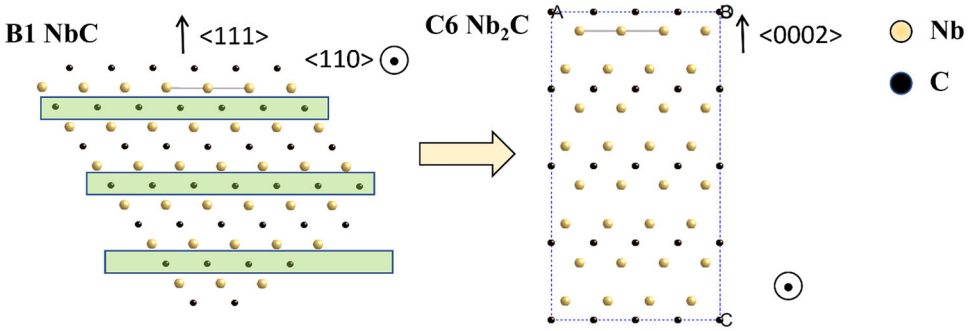

Fig. 5. A schematic illustration of the alternating Nb and C close-packed planes where those C planes in the designated green box are depleted allowing the schematic image on the right to fault and form the C6 structure (Color figure online).

hemicarbide,[39] where niobium and tantalum are in the same group VB transition metal family. The C6 structure can form from the B1 structure by depleting carbon from its {111} planes. When the B1 structure is viewed in the < 110> orientation, the {111} planes are normal to this direction and consist of alternating layers of metal and carbon close-packed planes (Fig. 5). Hence, the C6 structure forms by depleting every other {111} carbon plane in NbC, which achieves the correct composition, whereupon the depletion of carbon causes the two metal layers to collapse and shift by a Shockley partial dislocation to give the correct structure.[4] Since the B1 NbC_x structure has a high density of stacking faults, it is plausible that the carbon depletion from the rocksalt structure creates a condition whereupon the C6 structure forms from the prevalence of these stacking faults. A particularly interesting feature of the C6 structure is a local metal–metal as well as metal–carbon bond in the unit cell between the close-packed planes. This can be seen in the transformed structure shown in the schematic of Fig. 5. Prior work by De Leon et al.,[40] in C6 Ta_2C, has shown that a significant reduction in the generalized stacking fault energy exists between these two types of bonds, with the metal–metal being the lowest and energetically favorable plane for slip.[41] Returning to Fig. 2b, we can see that region 1, which is the C6 structure, is abutted to a NbC grain with a high density of linearly aligned stacking faults. While other transitory stacking fault phases may also exist, such as Nb_4C_{3-x}, it is difficult to distinguish their phase reflections from those collected in a highly faulted region. While this grain was C6 and likely formed from NbC, the precipitation of Nb_2C by carbon reacting with elemental Nb is different. In our prior work, where we focused on the carbon reaction front into Nb, we observed the direct precipitation of the ε–Fe_2N structure.[20]

To gain further insights into the energetics of this C6 Nb_2C transformation, we re-examine the stability of the Nb_2C structure using DFT with an emphasis to those structures that have a hexagonal

Table II. Structure and atomistic computed energies

Structure	Space group	Cohesive energy (eV/F.U.)	ΔE relative to ζ-Nb_2C (eV/F U)
ζ-Nb_2C	Pnma	23.251	0
ζ-Fe_2N	Pbcn	23.218	0.033
C6	$P\bar{3}m1$	23.204	0.047
e-Fe_2N	$P\bar{3}1m$	23.218	0.033
C35	Pnnm	23.234	0.017
C4	P4/mnm	23.035	0.216

close-packed arrangement of the atoms, as well as the C4 (rutile) structure, which is related to the C35 structure.[13] Using the enthalpy of formation as the metric for structural stability, the ζ-Nb_2C structure is predicted to be the lowest Nb_2C phase at 0 K (Table II). The next lowest energy structure is the C35 structure, while the C6 structure has the second highest energy next to the C4 structure. These energies are reported per formula unit and can easily be converted to per atom by dividing by three, which would indicate that the energy per atom difference between ζ-Nb_2C and the C6 structure is almost 0.015 eV/atom. This energy difference cannot be ignored and would specify that the identified C6 Nb_2C has not reached its equilibrium state but must be a transitory structure that forms in the reaction pathway toward equilibrium. This would follow the microstructure indicator of prevalent stacking faults already noted in NbC_x. The retention of the C6 structure is then likely linked to insufficient time for the correct ordering of the carbon atoms via diffusion.

CONCLUSION

An overall $Nb_{0.56}C$ composition carbide was hot isostatically pressed from a mixture of NbC and Nb powders. While the overall composition places it in a single Nb_2C phase field, incomplete homogenization occurred, allowing one to decipher how the B1 NbC structure evolves as the carbon is depleted. While Nb_2C has three reported polymorphs (α, β, and γ), none of these structures were observed in the SAED patterns taken from the examined foils. Rather, the NbC_x regions revealed a prevalence of stacking faults with an identified grain with no faults as the C6 structure next to a region composed of a high density of faults in NbC_x. To the authors' knowledge, this would be the first report of this structure for a niobium hemicarbide. While other stacking fault phases could also be present as transitory structures, these were difficult to distinguish in the SAED patterns from the reflections already created by a high density of faults. As the carbon depleted from the NbC, facilitating faulting, this 'liberated' carbon reacted with the Nb powder and has previously been reported to precipitate the ε–Fe_2N niobium hemicarbide structure.[20] These new results here demonstrate that the NbC_x can undergo a different transformation pathway towards stabilizing Nb_2C, evident from prevalent stacking fault formations that appear to promote the metastable formation of the C6 structure. In addition, the neutron diffraction, which samples multiple grains, has overlapping matching to previously reported stabilized niobium hemicarbides, and thus the C6 structure is likely not the only hemicarbide phase. This highlights the complexity of phase stability in the niobium hemicarbides, and that their structure is not only sensitive to temperature changes but to the processing pathways that form them.

ACKNOWLEDGEMENTS

G.B. T. recognizes NSF-DMR-2026760 and C.R.W. recognizes NSF-DMR-2026766 for support of this research. Stephen DiPeitro is thanked for the niobium hemicarbide sample. This research used resources at the Missouri University Research Reactor (MURR).

AUTHOR CONTRIBUTION

IB performed the electron microscopy and provided the first draft. JLP provided data analysis of the neutron diffraction data set. LDS also provided data analysis as well as performed neutron diffraction. CRW conducted the DFT simulations. CRW and GBT conceptualized the project, and provided technical direction and edits to the manuscript.

CONFLICT OF INTEREST

On behalf of all authors, the corresponding author states that there is no conflict of interest.

APPENDIX

See Fig. 6.

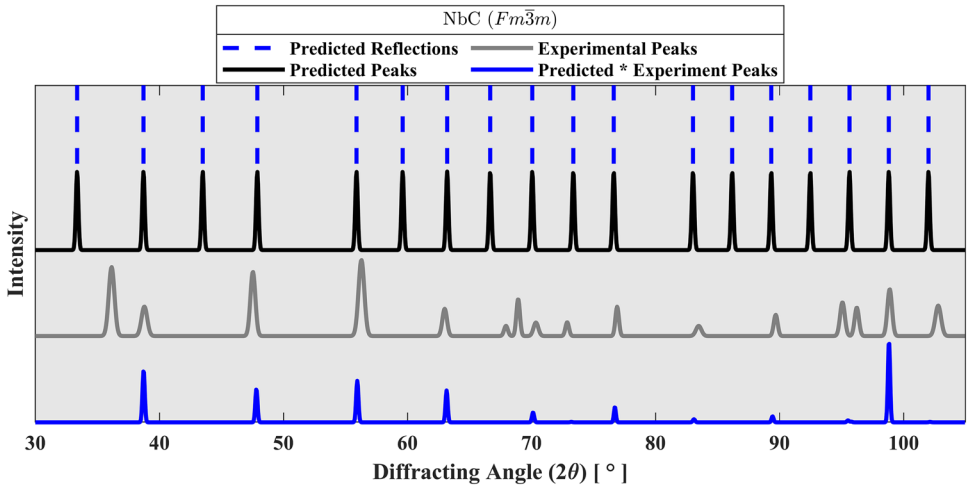

Fig 6. Illustration of the method to achieve the combined (predicted * experiment) peaks. The predicted reflections are calculated using known mathematical relationships for diffraction from crystal structures. Those reflections are replaced by Gaussian normal distributions, to achieve the predicted peaks. Then, the predicted and experimental peaks curves are multiplied (element wise) and normalized to yield the combined peaks curve.

REFERENCES

1. D.H. Jack, and K.H. Jack, *Mater. Sci. Eng.* 11(1), 1 https://doi.org/10.1016/0025-5416(73)90055-4 (1973).
2. E.K. Storms, and N.H. Krikorian, *J. Phys. Chem.* 64(10), 1471 https://doi.org/10.1021/j100839a029 (1960).
3. E. Rudy, S. Windisch, and C.E. Brukl, *Planseeber. Für Pulvermet.* 16, 3 (1968).
4. C.R. Weinberger, and G.B. Thompson, *J. Am. Ceram. Soc.* 101(10), 4401 https://doi.org/10.1111/jace.15768 (2018).
5. L. Wu, Y. Wang, Z. Yan, J. Zhang, F. Xiao, and B. Liao, *J. Alloy. Compd.* 561, 220 https://doi.org/10.1016/j.jallcom.2013.01.200 (2013).
6. J.P. Landesman, A.N. Christensen, C.H. de Novion, N. Lorenzelli, and P. Convert, *J. Phys. C Solid State Phys.* 18, 809 https://doi.org/10.1088/0022-3719/18/4/012 (1985).
7. A.I. Gusev, and A.A. Rempel', *Fizika Tverdogo Tela.* 26, 3622 (1984).
8. S.I. Alyamovskii, G.P. Shveikin, P.V. Geld, and N.M. Volkova, *Russ. J. Inorg. Chem.* 12, 301 (1967).
9. X.X. Yu, C.R. Weinberger, and G.B. Thompson, *Comput. Mater. Sci.* 112, 318 https://doi.org/10.1016/j.commatsci.2015.10.038 (2016).
10. S.S. Ordan'yan, A.I. Avgustinik, and L.V. Kudryasheva, *Soviet Powder Metall. Metal. Ceram.* 7, 612 https://doi.org/10.1007/BF00780218 (1968).
11. C.R. Weinberger, and G.B. Thompson, *Acta Cryst.* 75, 870 https://doi.org/10.1107/S2052520619011302 (2019).
12. H. Wiesenberger, W. Lengauer, and P. Ettmayer, *Acta Mater.* 46, 651 https://doi.org/10.1016/S1359-6454(97)00204-8 (1998).
13. X. Sha, N. Xiao, Y. Guan, and X. Yi, *RSC Adv.* 7, 33402 https://doi.org/10.1039/c7ra05856j (2017).
14. E. Rudy, and C.E. Brukl, *J. Am. Ceram. Soc.* 50, 265 https://doi.org/10.1111/j.1151-2916.1967.tb15101.x (1967).
15. M. Uz, and R.H. Titran, *AIP Conf. Proc.* 271(1), 69https://doi.org/10.1063/1.43076 (2008).
16. B. Vishwanadh, K.V.M. Krishna, A. Upadhyay, R. Banerjee, A. Arya, R. Tewari, H.L. Fraser, and G.K. Dey, *Acta Mater.* 108, 186 https://doi.org/10.1016/j.actamat.2016.02.036 (2016).
17. B. Vishwanadh, T.S.R.C. Murthy, A. Arya, R. Tewari, and G.K. Dey, *J. Alloy. Compd.* 671, 424https://doi.org/10.1016/j.jallcom.2016.02.092 (2016).
18. B. Lönnberg, and T. Lundström, *J. Less-Common Metals.* 113(2), 261https://doi.org/10.1016/0022-5088(85)90284-X (1985).
19. T. Epicier, J. Dubois, C. Esnouf, G. Fantozzi, and P. Convert, *Physica B* 156–157, 44https://doi.org/10.1016/0921-4526(89)90581-4 (1989).
20. C.J. Smith, C.R. Weinberger, and G.B. Thompson, *J. Eur. Ceram. Soc.* 38(15), 4850https://doi.org/10.1016/j.jeurceramsoc.2018.06.041 (2018).
21. Y. Zhou, T.W. Heitmann, E. Bohannan, J.C. Schaeperkoetter, W.G. Fahrenholtz, and G.E. Hilmas, *J. Am. Ceram. Soc.* 103, 2891 https://doi.org/10.1111/jace.16964 (2020).
22. V. Moisy-Maurice, C.H. de Novion, A.N. Christensen, and W. Just, *Solid State Commun.* 39, 661 https://doi.org/10.1016/0038-1098(81)90345-8 (1981).
23. J. Mayer, L.A. Giannuzzi, T. Kamino, and J. Michael, *MRS Bull.* 32(5), 400 https://doi.org/10.1557/mrs2007.63 (2007).
24. J. Rodríguez-Carvajal, *IUCr. Newsl.* 26, 12 (2001).
25. G. Kresse, and J. Hafner, *Am. Phys. Soc.* 47(1), 558 https://doi.org/10.1103/PhysRevB.47.558 (1993).
26. G. Kresse, and J. Furthmüller, *Am. Phys. Soc.* 54(16), 11169 https://doi.org/10.1103/PhysRevB.54.11169 (1996).
27. P.E. Blöchl, *Am. Phys. Soc.* 50(24), 17953 https://doi.org/10.1103/PhysRevB.50.17953 (1994).
28. G. Kresse, and D. Joubert, *Phys. Rev. B* 59, 1758 https://doi.org/10.1103/PhysRevB.59.1758 (1999).
29. J.P. Perdew, K. Burke, and M. Ernzerhof, *Phys. Rev. Lett.* 77, 3865 https://doi.org/10.1103/PhysRevLett.77.3865 (1996).
30. D. Rechenbach, and H. Jacobs, *J. Alloy. Compd.* 235(1), 15https://doi.org/10.1016/0925-8388(95)02097-7 (1996).
31. K. Yvon, H. Nowotny, and R. Kieffer, *Monatshefte für Chemie und verwandte Teile anderer Wissenschaften* 98(1), 34 https://doi.org/10.1007/BF00901093 (1967).
32. E. Rudy, F. Benesovsky, and K. Sedlatschek, *Monatshefte für Chemie und verwandte Teile anderer Wissenschaften* 92(4), 841 https://doi.org/10.1007/BF01187680 (1961).
33. A.V. Skripov, H. Wu, T.J. Udovic, Q. Huang, and R. Hempelmann, *J. Alloy. Compd.* 478(1), 68 https://doi.org/10.1016/j.jallcom.2008.12.012 (2009).
34. C.J. Howard, B.J. Kennedy, and C. Curfs, *Phys. Rev. B* 72(21), 214114https://doi.org/10.1103/PhysRevB.72.214114 (2005).
35. K. Yvon, and E. Parthé, *Acta Crystallogr. B* 26(2), 149https://doi.org/10.1107/s0567740870002091 (1970).
36. K. Nakamura, and M. Yashima, *Mater. Sci. Eng., B* 148(1), 69https://doi.org/10.1016/j.mseb.2007.09.040 (2008).
37. H.G. Schimmel, J. Huot, L.C. Chapon, F.D. Tichelaar, and F.M. Mulder, *J. Am. Chem. Soc.* 127(41), 14348 https://doi.org/10.1021/ja051508a (2005).

38. W.G. Fahrenholtz, E.J. Wuchina, W.E. Lee, Y. Zhou, editors. Ultra-High Tempeature Ceramics: Materials for Extreme Environment Applications, *The American Ceramic Society*, (2014). https://doi.org/10.1002/9781118700853.
39. X.X. Yu, C.R. Weinberger, and G.B. Thompson, *Acta Mater.* 80, 341 https://doi.org/10.1016/j.actamat.2014.07.070 (2014).
40. N. De Leon, B. Wang, C.R. Weinberger, L.E. Matson, and G.B. Thompson, *Acta Mater.* 61(11), 3905 https://doi.org/10.1016/j.actamat.2013.01.043 (2013).
41. B. Wang, N. De Leon, C.R. Weinberger, and G.B. Thompson, *Acta Mater.* 61(11), 3914 https://doi.org/10.1016/j.actamat.2013.01.047 (2013).